Communication

ZIF-75 under Pressure: Negative Linear Compressibility and Pressure-Induced Instability

Francisco Colmenero [1,2,*] and Vicente Timón [2]

[1] Departamento de Química-Física, Facultad de Ciencias Químicas, Universidad Complutense de Madrid, 28040 Madrid, Spain
[2] Instituto de Estructura de la Materia (IEM), Consejo Superior de Investigaciones Científicas, 28006 Madrid, Spain
* Correspondence: francolm@ucm.es

Featured Application: The zeolitic imidazolate framework ZIF-75 exhibits the negative linear compressibility effect under small applied pressures with multiple potential applications.

Abstract: The behavior of the crystal structure of the zeolitic imidazolate framework ZIF-75 under pressure was studied by means of periodic density functional theory methods. Experimentally, it was shown that this material is tetragonal, space group $I41/a$, at room temperature. However, according to the calculations, at zero temperature this material is monoclinic, space group $C2/c$. Irrespective of the symmetry of the material, the results show that ZIF-75 exhibits a negative linear compressibility effect and is unstable under relatively small applied pressures of the order of 0.1 GPa.

1. Introduction

Zeolitic imidazolate frameworks (ZIF) [1–4] are a unique class of metal–organic frameworks (MOFs) [5]. MOF materials are important porous coordination polymers synthesized from metal building units bridged by organic ligands. ZIFs are constructed from tetrahedrally coordinated cations, typically zinc or cobalt, linked by imidazolate derivatives. These compounds have exceptional properties, such as their large chemical and thermal stability [1], and unusual structural properties, such as their large pore size and accessible surface. These characteristics mean that these materials are appropriate for a large series of technological and industrial applications, such as gas and compound adsorption [6–11], separation [4,7,12–15], and storage [10,16,17]; catalysis [4,7,18–22]; drug delivery [23]; and sensor and device development [24–28]. Furthermore, these compounds are highly flexible and sensitive to the action of pressure [29–45]. These properties make them appropriate for a large spectrum of additional applications [46–49,23], such as in mechanical damping and mechanical energy storage [50–57], and may enhance their applicability for other applications, such as compound adsorption and separation and catalysis. This is because the deformation or their pore structure brought by the action of the pressure may increase their sorption capacity and selectivity and facilitate access to the binding sites [9–11,29–32,45,58,59].

The crystal structures resulting from the linkage of the metal cations and imidazolate ligands in ZIFs [1–4] result in porous structures with topologies analogous to those of MOFs, aluminosilicates, and zeolites [5]. The application of high pressures on highly porous materials also has importance in synthetic chemistry since it has allowed the design of new advanced functional materials such as amorphous materials, glasses, and crystalline compounds from structural rearrangements and phase transitions induced by

pressure [60–66]. Therefore, the detection of pressure-induced instabilities in porous materials is also of practical importance. The pressure-induced amorphization in ZIF-8 has long been investigated [11,29,30,32,38,44], and the detection of pressure-induced phase transitions and amorphizations in other ZIF materials could be extremely interesting. Additional potential applications for microporous materials are possible because these materials frequently appear to exhibit the negative linear compressibility [45,67–83] and negative Poisson's ratio [81,84–87] phenomena. These phenomena [88–91] have multiple potential applications in the development of ultrasensitive pressure-sensing devices [88,92], pressure-driven actuators [92,93], optical telecommunication cables [88], artificial muscles [94], and body armor [92,95], as well as sound attenuation [96], superconductivity modulation [97], ferroelectric enhancement [88], and transmission stabilization [98]. However, for the evaluation of the suitability of these compounds for practical, specific applications, the behavior of their structures under the effect of pressure must be investigated. The study of the mechanical properties of microporous compounds has been the subject of a large amount of research in recent decades [29–45,67–87]. The first principles solid-state methodology have been satisfactorily applied for this purpose and have enhanced our knowledge of the mechanical properties of these materials since they give access to the full tensorial elasticity of these materials [34–37,67–70,81–83,86,87,99–108]. The results obtained using the *state-of-the-art* theoretical methodology are consistently in agreement with the experiment, even for the theoretical study of complex anomalous negative mechanical phenomena [81–83,102–108] and for crystal structure determination [109–113]. For example, the negative area compressibility of silver oxalate, predicted using first-principles methods [107], was recently experimentally verified [108]. The ZIF material, ZIF-75, was synthetized for the first time by Tian et al. [2]. Its structure shows the presence of large structural channels; therefore, it should be extremely useful in various applications due to the large pore space and accessible surface. However, as far as we know, it has not been used in practical applications and its behavior under pressure has not been investigated.

2. First-Principles Methods

The crystal structure and the behavior of the zeolitic imidazolate framework ZIF-75 [2,3] (CCDC code HIFVUO and deposition number 254162) under pressure were modeled by employing periodic density functional theory methods using plane-wave-basis sets and pseudopotentials [114]. The CASTEP (Cambridge Serial Total Energy Program) computer program [115], belonging to the Materials Studio program suite [116], was utilized in all the calculations. The specific energy density functional employed in the computations is the Perdew–Burke–Ernzerhof (PBE) functional [117] supplemented with Grimme dispersion corrections [118], as implemented in the CASTEP code. The pseudopotentials utilized for all the atoms in the unit cell of ZIF-75 were standard norm-conserving pseudopotentials [119] provided in the CASTEP code (00PBE-OP type). The calculations were performed using demanding calculation parameters: a cut-off for the kinetic energy of the plane waves of 1000 eV and a Monkhorst–Pack k-mesh [120] with a grid density of 0.4 $Å^{-1}$. The full-geometry optimization, including the atomic positions and unit cell lattice parameters, was performed using the Broyden–Fletcher–Goldfarb–Shanno (BFGS) method [121]. All the optimizations, including those of ZIF-75 under pressure, were performed with stringent convergence thresholds in the variation of the total energy, maximum atomic displacement, maximum atomic force, and maximum stress: 2.5×10^{-6} eV/atom, 2.5×10^{-4} Å, 0.005 eV/Å, and 0.0025 GPa, respectively. The geometry optimizations were performed using the crystal structure reported by Tian et al. [2] as a starting point, and, as customary, they were performed by relaxing all symmetry constraints for the verification of the adopted crystallographic space symmetry group. Since the unit cell of ZIF-75 is very large, containing 272 atoms, the symmetry-unrestricted full-geometry optimizations are computationally expensive. The X-ray powder-diffraction patterns [122] of ZIF-75 were derived from the computed and experimental crystal structures using software REFLEX included in the Materials Studio program suite [116] using CuK$_\alpha$

radiation ($\lambda = 1.540598$ Å). The elasticity constants, that is, the elements of the elastic tensor of ZIF-75, were determined in the optimized crystal structure using the finite deformation method (FDM) [123]. This technique is highly efficient and reliable for describing the elastic response of materials and has been employed successfully in many previous works concerning uranium-containing materials [109–113] as well as organic crystals [102–104] and metal–organic compounds [81–83,105–107,124]. In particular, the elasticity of a wide variety of MOFs and microporous materials has been studied [81–83].

3. Results

3.1. Crystal Structure

The computed crystal structure of ZIF-75 is shown in Figure 1. According to Tian et al. [2], ZIF-75 is tetragonal, space group $I41/a$. The composition of the unit cell of the framework is $Zn(Im_2)$, where the imidazolate ligand has molecular formula $Im \equiv C_3H_2N_2$. The structure of the imidazolate ligand is shown in Figure 2. According to Phan et al. [3] and the *Reticular Chemistry Structure Resource (RSCR)* [125], ZIF-75 belongs to GIS topology and has the zeolite code GIS. The size of the diameter of the largest sphere that will fit into the channels without contacting the framework atoms is 8.6 Å. As can be observed, the crystal structure of ZIF-75 contains large empty channels expanding along the [1 0 0] direction of two types. The main channels are shown at the center of Figure 1, and the secondary ones are shown on the left- and right-hand sides of the main channels. The main channels are very large, having horizontal and vertical dimensions of $\omega = 10.6$ and $h = 7.0$ Å, respectively, as measured by the distance between opposite hydrogen atoms (see Figure 1).
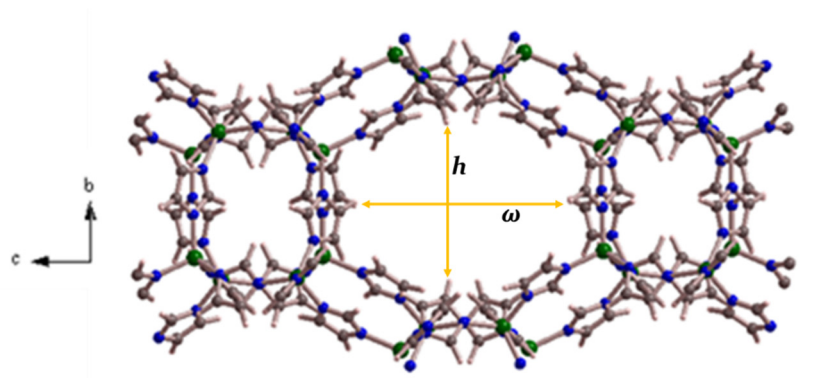
Figure 1. View of crystal structure of ZIF-75 from [1 0 0] crystallographic direction. The meaning of the horizontal and vertical dimensions of the main channels in ZIF-75, ω and h, is also explained in the figure. Color code: Zn—green; N—blue; C—gray; H—white.
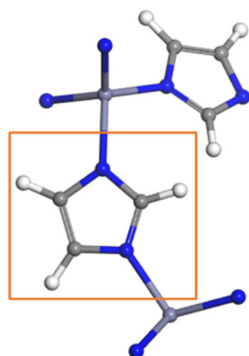
Figure 2. The structure of the imidazolate ligand. The ligand is shown within an orange box. As observed in the figure, the ligand may link with other carbon atoms through the N atoms. Color code: N—blue; C—gray; H—white.

The computed lattice parameters of ZIF-75 are shown in Table 1. As can be seen in the second row of Table 1, the unit cell parameters of ZIF-75 are well-reproduced despite the complexity and large size of the unit cell of this framework material. The computed unit cell volume overestimates the experimental one by 11.4%. The inclusion of dispersion corrections is fundamental for ZIF-75 as the uncorrected PBE functional (first row of Table 1) leads to an extremely large overestimation of the lattice parameters. The PBE unit cell volume overestimation is huge, at 32.4%. As mentioned in the Methods Section, the geometry optimizations were in fact performed first, relaxing all symmetry constraints. The tetragonal symmetry was broken and, by finding the space symmetry of the resulting optimized structure, a monoclinic symmetry, space group ($C2/c$), was found. The unit cell parameters of the fully optimized monoclinic structure are given in the third row of Table 1. This structure is reported in the Supplementary Material of this paper as a file in the CIF (crystallographic information file) file format. While the bonding structure in the monoclinic structure is analogous to that of the tetragonal one, the difference in the unit cell volumes is about 8 Å^3 and the monoclinic structure is more stable than the tetragonal one with a difference of enthalpy of about 3.9 Kcal·mol^{-1}. We cannot claim that the tetragonal space symmetry of ZIF-75 is not correct since the structure was determined by Rietveld refinement from powder X-ray diffraction data at room temperature (293 K), and the results of the present calculations refer to zero temperature. The Rietveld refinement of X-ray diffraction data at low temperatures could be used to verify the theoretical result.

Table 1. Computed unit cell parameters of ZIF-75.

Parameter	a (Å)	b (Å)	c (Å)	α (deg)	β (deg)	γ (deg)	Vol. (Å^3)	ρ(g/cm^3)
PBE ($I41/a$)	19.7016	19.7016	19.3796	90.0	90.0	90.0	7522.2774	0.7047
PBE+Disp ($I41/a$)	19.1356	19.1356	19.6719	90.0	90.0	90.0	7203.3094	0.7359
PBE+Disp ($C2/C$)	26.6209	19.7885	19.1182	90.0	134.32	90.0	7212.9116	0.7350
Exp. [2] ($I41/a$)	18.389 (4)	18.389 (4)	19.129 (5)	90.0	90.0	90.0	6469 (2)	0.819

The volume and enthalpy differences for the structures having tetragonal ($I41/a$) and monoclinic ($C2/c$) structures of ZIF-75 are rather small. The description of the behavior under pressure of ZIF-75 in the full range of pressure studied (from $P = -1.0$ to 1.0 GPa) is analogous. Therefore, the results provided in the next sections were obtained using the tetragonal structure, but it must be emphasized that essentially the same conclusions were obtained independently of the space symmetry employed.

The X-ray diffraction patterns of ZIF-75 were obtained using tetragonal experimental [2] and theoretical structures, employing CuK$_\alpha$ radiation (λ = 1.540598 Å). The resulting patterns are compared in Figure 3. As observed, both patterns are in excellent agreement. A more detailed comparison of the positions of the most important reflections in both patterns is given in Table S1 of the Supplementary Materials. As can be seen, the differences in these positions are small, with the largest difference being found for reflection [1 5 4], Δ = 1.11°. The X-ray diffraction pattern of the computed monoclinic structure was also determined. A comparison of the patterns associated with the computed monoclinic and tetragonal crystal structures is given in Figure S1 of the Supplementary Materials. Both patterns are also in good agreement and are consistent with the pattern derived from the experimental tetragonal structure.
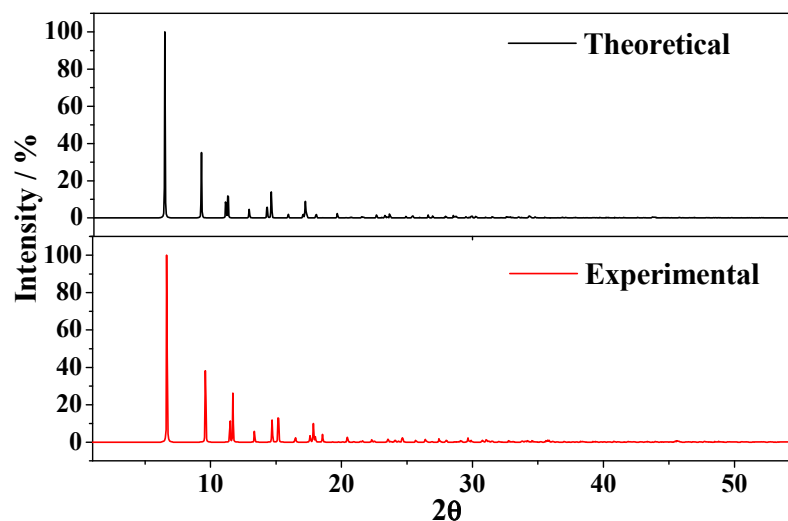
Figure 3. Comparison of the X-ray diffraction patterns of ZIF-75 derived from the experimental [2] and theoretical tetragonal crystal structures.

3.2. Elasticity Tensor and Mechanical Stability

The computed elasticity tensor for ZIF-75 is given in Equation (1). Crystals of the tetragonal space group $I41/a$ belong to the tetragonal (II) class (4/m). In this case, the elastic tensor has only 11 nonvanishing elastic constants, of which only six are independent [126] ($C_{11} = C_{22}$; $C_{44} = C_{55}$; $C_{13} = C_{23}$; $C_{16} = -C_{26}$;).

$$C = \begin{pmatrix} 5.22 & 3.45 & 10.17 & 0.00 & 0.00 & 0.04 \\ 3.45 & 5.22 & 10.17 & 0.00 & 0.00 & -0.04 \\ 10.17 & 10.17 & 13.35 & 0.00 & 0.00 & 0.00 \\ 0.00 & 0.00 & 0.00 & 0.36 & 0.00 & 0.00 \\ 0.00 & 0.00 & 0.00 & 0.00 & 0.36 & 0.00 \\ 0.00 & 0.00 & 0.00 & 0.00 & 0.00 & -0.29 \end{pmatrix} \tag{1}$$

For a given material, the general Born condition for mechanical stability is that the corresponding elastic matrix should be positive definite [126], i.e., all the eigenvalues of the elastic matrix should be positive. For crystals belonging to the tetragonal (II) class (4/m), there is a simple set of equivalent conditions for mechanical stability [126]:

$$C_{11} > |C_{12}| \tag{2}$$

$$2 \cdot C_{13}^2 > (C_{11} + C_{12}) \tag{3}$$

$$C_{44} > 0 \tag{4}$$

$$2 \cdot C_{16} > C_{66}(C_{11} - C_{12}) \tag{5}$$

The last condition is not satisfied; therefore, the crystal structure of ZIF-75 is not mechanically stable. The reason for the mechanical instability of ZIF-75 will be unveiled in the next section, where the deformation of its crystal structure under pressure is investigated.

3.3. Behavior of ZIF-75 under the Effect of Pressure. Pressure-induced Phase Transition and Negative Linear Compressibility

The crystal structure of ZIF-75 was fully optimized under the effect of 14 different isotropic pressures within the range going from $P = -1.0$ to 1.0 GPa. The computed lattice parameters and unit cell volumes at these pressures are tabulated in Table S3 of the Supplementary Materials and plotted in Figure 4. As can be clearly seen, the effect of pressure induces a phase transition at a pressure near $P = 0.1$ GPa. The presence of this pressure-

induced phase transition at a small pressure close to zero GPa is the main reason for the mechanical instability in ZIF-75, as found in Section 3.2.
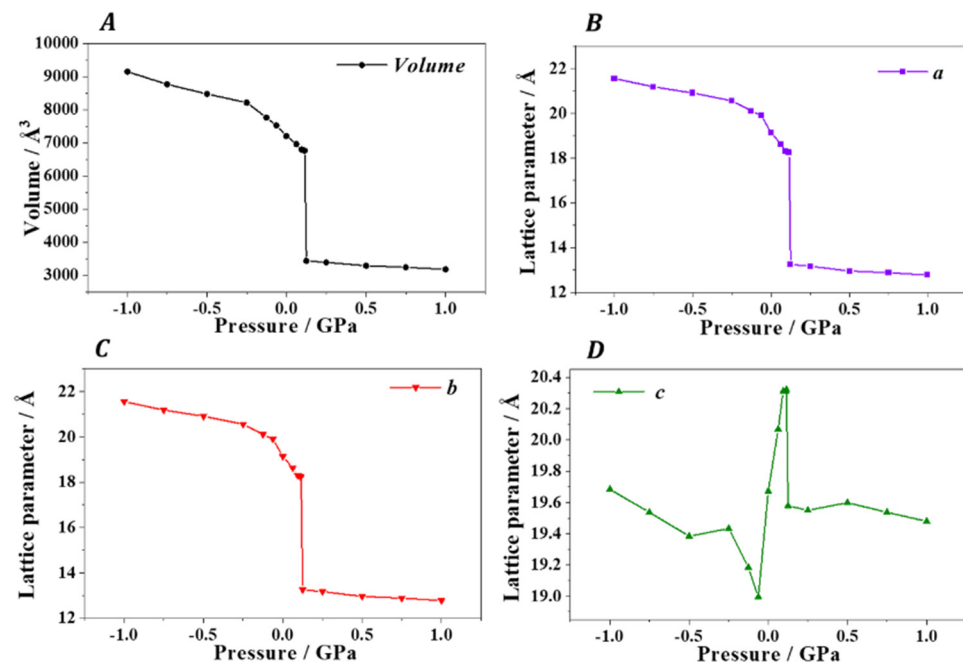
Figure 4. Computed unit cell volumes and lattice parameters of ZIF-75 as a function of the applied isotropic pressure: (**A**) unit cell volume; (**B**) a lattice parameter; (**C**) b lattice parameter; (**D**) c lattice parameter.

From the computed elasticity matrix, the dependence of the compressibility of ZIF-75 as a function of the orientation of the external pressure was obtained and plotted on the ElAM computer program [127]. As can be seen in Figure 5, the compressibility is negative for uniaxial pressures applied in any direction contained in the (1 1 0) plane. As it will be shown, indeed, the compressibility along c direction is also negative when ZIF-75 is submitted to isotropic pressures.
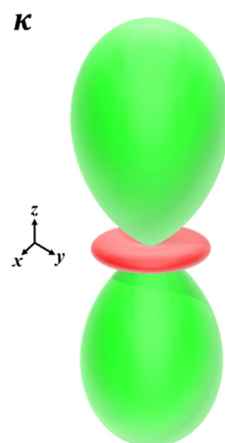
Figure 5. Compressibility of ZIF-75 as a function of the applied strain. The negative and positive values are displayed in red and green, respectively.

As can be observed in Figure 4, the behavior of the a and b lattice parameters, while presenting a rapidly decreasing behavior near the phase transition, is normal in the sense that they decrease invariably along the full pressure range. However, the c lattice parameter presents an anomalous behavior and sharply increases before the phase transition in

the pressure range going from $P = -0.06$ to 0.1 GPa. Therefore, ZIF-75 presents a remarkable negative linear compressibility effect in this pressure range since the linear compressibility along the c direction, $k_c = -1/c \cdot (\partial c/\partial P)_P$, is strongly negative.

4. Discussion

The elasticity matrix of ZIF-75 was determined at the equilibrium crystal structure employing the FDM technique. The study of the mechanical stability of ZIF-75 showed that it is unstable. The reason for the mechanical instability of ZIF-75 was unveiled by the examination of the variation of the computed crystal structures under the effect of pressure, showing that ZIF-75 undergoes a pressure-induced phase transition at very small applied pressures of $P \approx 0.1$ GPa.

Furthermore, the study of the variation of the unit cell parameters under pressure showed that the behavior of the c lattice parameter is anomalous. It strongly increases in the pressure range from $P = -0.06$ to 0.1 GPa; therefore, ZIF-75 presents the negative linear compressibility phenomenon in this range of pressure. The modifications of the crystal structures were analyzed in order to study the structural mechanism leading to the presence of the phenomenon of negative linear compressibility. The inspection of the deformation of these structures as the pressure increases led to the conclusion that the NLC phenomenon in ZIF-75 can be understood by employing the empty channel structural mechanism [81–83,128]. The modifications of the structure of ZIF-75 at four different pressures, $P = -0.0625, 0.0, 0.0625$, and 0.125 GPa, are shown in Figure 6.
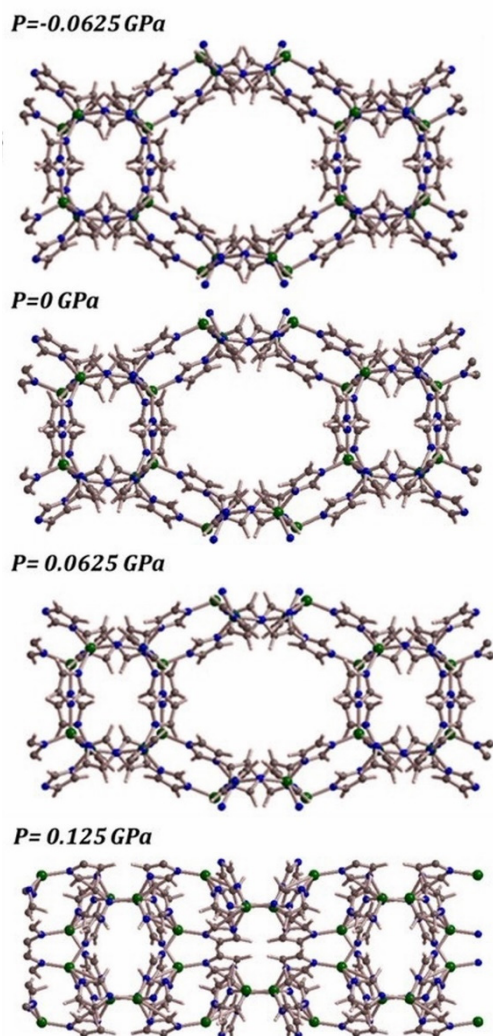
Figure 6. View of crystal structure of ZIF-75 from [1 0 0] crystallographic direction at four different pressures, P = −0.0625, 0.0, 0.0625, and 0.125 GPa. The subfigure corresponding to P = 0.125 GPa provides a view of the crystal structure after the pressure-induced phase transition. Color code: Zn—green; N—blue; C—gray; O—red; H—white.

In microporous materials exhibiting empty structural channels, the application of isotropic pressure may lead to a flattening of the channels which become wider along the direction of the largest semiaxis in a section perpendicular to the channels and shorter in the perpendicular direction. The widening of the channels in turn leads to the increase in the corresponding lattice parameter, which in the present case is the c lattice parameter. This mechanism, described for the first time in 2020, has been found to be responsible for the NLC phenomenon in several different microporous materials [81–83,128]. The last crystal structure of ZIF-75 shown in Figure 6, corresponding to an applied pressure of P = 0.125 GPa, is, as expected, completely different from the other ones because this pressure is well beyond the phase transition pressure. In this structure, the presence of smaller structural empty channels expanding along the [0 0 1] direction is still observed. The new material generated through the pressure-induced transition must have completely different properties to those of ZIF-75 and may be functional for other applications. The reversibility of the phase transition upon the removal of the effect of pressure and properties of the new material should be experimentally investigated in detail.

A large set of ZIF materials were selected for this study, such as those synthetized by Park et al. [1] and Tian et al. [2]. We were looking for microporous materials exhibiting large empty structural channels, which, according to previous studies [81–83,128], are likely to exhibit the negative linear compressibility phenomenon. Due to the large size of its structural channels, ZIF-75 was selected among the studied ZIF materials. Therefore, it was a good candidate for the study of its behavior under pressure. Furthermore, the initial exploratory test calculations of this material showed that, indeed, its behavior under pressure was very interesting. For comparison, as far as we know, a pressure-induced instability was only found for the ZIF-8 material [11,29,30,32,38,44] at about 0.34 GPa [29], which has long been investigated.

The behavior of ZIF-75 material under pressure has never been investigated experimentally. The presence of the pressure-induced phase transition in ZIF-75 was detected using the first-principles solid-state methods; therefore, it should be experimentally verified. Furthermore, the results obtained in this work concern the behavior under pressure of a single ZIF-75 crystal, whereas the experimental measurements generally correspond to a polycrystalline aggregate of many crystals. However, the results obtained with high-quality calculations using the *state-of-the-art* theoretical methods are consistently in good agreement with the experimental results in the cases in which the theoretical methods have been compared against available experimental data (for example, for silver oxalate [107,108], oxalic acid and succinic acid [103,104,129], MIL-53 [69,70,73], and MIL-47 [130]). Following previous studies [107,108], powder samples of ZIF-75 could be synthetized according to, for example, the synthetic methods used by Tian et al. [2]. Then, these samples could be used to obtain the corresponding powder X-ray diffraction patterns under different pressures. From them, the lattice parameters or even the full crystal structures could be determined by refinement from the X-ray diffraction data. Then, the analysis of the variation of the parameters should reveal the presence of the NLC effect as well as the onset of the pressure-induced phase transition.

Finally, it must be noted that the ZIF material studied in this work is ZIF-75 [2,3] (CCDC code HIFVUO and deposition number 254162). However, in some works (see for example [131]), the ZIF material with CCDC code HIFVUO is denoted as ZIF-6. This is a nomenclature error, as the ZIF-6 material has CCDC code EQOCOC01 and deposition number 602540 [1,3].

5. Conclusions

In this study, the behavior of the zeolitic imidazolate framework ZIF-75 under the effect of pressure was studied by means of periodic density functional methods using basis sets composed of plane waves and norm-conserving pseudopotentials. Initially, the structural results showed that, while at room temperature, ZIF-75 is tetragonal, space group I41/a; at zero temperature, ZIF-75 is monoclinic, space group C2/c. This result should be verified experimentally by the refinement of X-ray diffraction data at a low temperature. The study of the computed crystal structures under increasing pressures demonstrates that ZIF-75 undergoes a pressure-induced phase transition at relatively low pressures of $P \approx 0.1$ GPa. Furthermore, in the range of pressure going from $P = -0.06$ to 0.1 GPa, ZIF-75 exhibits the negative linear compressibility effect since the dimension of the crystal along the [0 1 0] crystallographic direction increases very rapidly as the pressure increases. This material may therefore be appropriate for many of the potential applications associated with the NLC effect. In this sense, one advantage of this material over other NLC materials [89] is its composition, since it does not contain metallic elements and its synthesis is relatively simple [2]. However, the presence of the pressure-induced phase transition limits the range of applicability of this material, not only in the applications where pressure plays a significant role but also in the most common applications in which the material operates under stressed conditions. One example is gas adsorption and storage, since the gas molecules' collisions with the walls of the channels may exert significant pressure on them [9,30,32,45,83].

The behavior of MOF materials under pressure is an extremely important topic from the point of view of their various applications. In summary, the results found in the present work are significant because they have shown, in the first place, that ZIF-75 undergoes a pressure-induced phase transition at small applied pressures near 1.0 GPa. The implications of this finding are twofold: (a) the new material obtained after the application of pressure, also microporous, may be a functional material, and the possible applications of this material should be experimentally investigated; (b) the presence of a pressure-induced phase transition limits the applicability of ZIF-75 in the common applications of this material, such as gas and compound absorption, separation, and storage, and catalysis, to pressures smaller than 1 GPa. Secondly, ZIF-75 exhibits a strong negative linear compressibility effect under applied pressures from $P = -0.06$ to 0.1 GPa, with a large series of potential applications.

References

1.   Park, K.S.; Zheng, N.; Cote, A.P.; Choi, J.Y.; Huang, R.; Uribe-Romo, F.J.; Chae, H.K.; O'Keeffe, M.; Yaghi, O.M. Exceptional chemical and thermal stability of zeolitic imidazolate frameworks. *Proc. Natl. Acad. Sci. USA* **2006**, *103*, 10186–10191.

2.   Tian, Y.Q.; Zhao, Y.M.; Chen, Z.X.; Zhang, G.N.; Weng, L.H.; Zhao, D.Y. Design and Generation of Extended Zeolitic Metal–Organic Frameworks (ZMOFs): Synthesis and Crystal Structures of Zinc(II) Imidazolate Polymers with Zeolitic Topologies. *Chem. Eur. J.* **2007**, *13*, 4146–4154.

3.   Phan, A.; Doonan, C.J.; Uribe-Romo, F.J.; Knobler, C.B.; O'Keeffe, M.; Yagui, O.M. Synthesis, Structure, and Carbon Dioxide Capture Properties of Zeolitic Imidazolate Frameworks. *Acc. Chem. Res.* **2010**, *43*, 58–67.

4.   Chen, B.; Yang, Z.; Zhu, Y.; Xia, Y. Zeolitic imidazolate framework materials: Recent progress in synthesis and applications. *J. Mater. Chem. A* **2014**, *2*, 16811–16831.

5.   Wright, P.A. *Microporous Framework Solids*; RSC Publishing: Cambridge, UK, 2008.

6.   Banerjee, R.; Phan, A.; Wang, B.; Knobler, C.; Furukawa, H.; O'Keeffe, M.; Yaghi, O.M. High-Throughput Synthesis of Zeolitic Imidazolate Frameworks and Application to CO_2 Capture. *Science* **2008**, *319*, 939–943.

7.   Zhong, G.; Liu, D.; Zhang, J. The application of ZIF-67 and its derivatives: Adsorption, separation, electrochemistry and catalysts. *J. Mater. Chem. A* **2018**, *6*, 1887–1899.

8.   Zhong, Y.; Mu, X.; Cheang, U.K. High-performance and selective adsorption of ZIF-8/MIL-100 hybrids towards organic pollutants. *Nanoscale Adv.* **2022**, *4*, 1431–1444.

9.   Kontos, A.G.; Romanos, G.E.; Veziri, C.M.; Gotzias, A.; Arfanis, M.K.; Kouvelos, E.; Likodimos, V.; Karanikolos, G.N.; Falaras, P. Correlating vibrational properties with temperature and pressure dependent to CO_2 adsorption in zeolitic imidazolate frameworks. *Appl. Surf. Sci.* **2020**, *529*, 147058.

10. Bose, R.; Ethiraj, J.; Sridhar, P.; Varghese, J.J.; Kaisare, N.S.; Selvam, P. Adsorption of hydrogen and carbon dioxide in zeolitic imidazolate framework structure with SOD topology: Experimental and modelling studies. *Adsorption* **2020**, *26*, 1027–1038.

11. Ma, Q.; Jin, J.; Li, Y. Tuning the Adsorption Selectivity of ZIF-8 by Amorphization. *Chem. Eur. J.* **2020**, *26*, 13137–13141.

12. Cacho-Bailo, F.; Etxeberría-Benavides, M.; David, O.; Téllez, C.; Coronas, J. Structural Contraction of Zeolitic Imidazolate Frameworks: Membrane Application on Porous Metallic Hollow Fibers for Gas Separation. *ACS Appl. Mater. Interfaces* **2017**, *9*, 20787–20796.

13. Wu, T.; Lucero, J.; Zong, Z.; Elsaidi, S.K.; Thallapally, P.K.; Carreon, M.A. Microporous Crystalline Membranes for Kr/Xe Separation: Comparison Between AlPO-18, SAPO-34, and ZIF-8. *ACS Appl. Nano Mater.* **2018**, *1*, 463–470.

14. Ma, Q.; Mo, K.; Gao, S.; Xie, Y.; Wang, J.; Jin, H.; Feldhoff, A.; Xu, S.; Lin, J.Y.S.; Li, S. Ultrafast Semi-Solid Processing of Highly Durable ZIF-8 Membranes for Propylene/Propane Separation. *Angew. Chem. Int. Ed.* **2020**, *59*, 21909–21914.

15. Bergaoui, M.; Khalfaoui, M.; Awadallah-F, A.; Al-Muhtase, S. A review of the features and applications of ZIF-8 and its derivatives for separating CO_2 and isomers of C_3- and C_4- hydrocarbon. *J. Nat. Gas Sci. Eng.* **2021**, *96*, 104289.

16. Wang, B.; Côté, A.P.; Furukawa, H.; O'Keeffe, M.; Yaghi, O.M. Colossal cages in zeolitic imidazolate frameworks as selective carbon dioxide reservoirs. *Nature* **2008**, *453*, 207–211.

17. Mu, L.; Liu, B.; Liu, H.; Yang, Y.; Sun, C.; Chen, G. A novel method to improve the gas storage capacity of ZIF-8. *J. Mater. Chem.* **2012**, *22*, 12246–12252.

18. Nguyen, L.T.L.; Le, K.K.A.; Truong, H.X.; Phan, N.T.S. Metal–organic frameworks for catalysis: The Knoevenagel reaction using zeolite imidazolate framework ZIF-9 as an efficient heterogeneous catalyst. *Catal. Sci. Technol.* **2012**, *2*, 521–528.

19. Nguyen, V.D.; Nguyen, C.K.; Tran, K.N.; Tu, T.N.; Nguyen, T.T.; Dang, H.V.; Truong, T.; Phan, N.T.S. Zeolite imidazolate frameworks in catalysis: Synthesis of benzimidazoles via cascade redox condensation using Co-ZIF-67 as an efficient heterogeneous catalyst. *Appl. Catal. A* **2018**, *555*, 20–26.

20. Oozeerally, R.; Ramkhelawan, S.D.K.; Burnett, D.L.; Tempelman, C.H.L.; Degirmenci, V. ZIF-8 Metal Organic Framework for the Conversion of Glucose to Fructose and 5-Hydroxymethyl Furfural. *Catalysts* **2019**, *9*, 812.

21. Hou, W.; Huang, Y.; Liu, X. Highly Efficient and Recyclable ZIF-67 Catalyst for the Degradation of Tetracycline. *Catal. Lett.* **2020**, *150*, 3017–3022.

22. Wen, H.; Zhang, S.; Yu, T.; Yia, Z.; Guo, R. ZIF-67-based catalysts for oxygen evolution reaction. *Nanoscale* **2021**, *13*, 12058–12087.

23. Wu, Y.; Cao, S.; Xuan, S.; Sang, M.; Bai, L.; Wang, S.; Zhang, J.; Wang, Y.; Jiang, W.; Gong, X. High performance zeolitic imidazolate framework-8 (ZIF-8) based suspension: Improving the shear thickening effect by controlling the morphological particle-particle interaction. *Adv. Powder Technol.* **2020**, *31*, 70–77.

24. Eslava, S.; Zhang, L.; Esconjauregui, S.; Yang, J.; Baklanov, K.M.; Saiz, M.R. Metal-organic framework ZIF-8 films as low-κ dielectrics in microelectronics. *Chem. Mater.* **2013**, *25*, 27–33.

25. Zhang, P.; Sun, F.; Shena, Z.; Cao, D. ZIF-derived porous carbon: A promising supercapacitor electrode material. *J. Mater. Chem. A* **2014**, *2*, 12873–12880.

26. Ma, Z.; Li, J.; Ma, R.; He, J.; Song, X.; Yu, J.; Quana, Y.; Wan, G. The methodologically obtained derivative of ZIF-67 metal–organic frameworks present impressive supercapacitor performance. *New J. Chem.* **2022**, *46*, 7230–7241.

27. Paul, A.; Banga, I.K.; Muthukumar, S.; Prasad, S. Engineering the ZIF-8 Pore for Electrochemical Sensor Applications. A Mini Review. *ACS Omega* **2022**, *7*, 26993–27003.

28. Qin, Y.; Xie, J.; Liu, S.; Bai, Y. Selective methanol-sensing of SnS-supported ultrathin ZIF-8 nanocomposite with core-shell heterostructure. *Sens. Actuators B Chem.* **2022**, *368*, 132230.

29. Chapman, K.W.; Halder, G.J.; Chupas, P.J. Pressure-Induced Amorphization and Porosity Modification in a Metal-Organic Framework. *J. Am. Chem. Soc.* **2009**, *131*, 17546–17547.

30. Moggach, S.A.; Bennett, T.D.; Cheetham, A.K. The Effect of Pressure on ZIF-8: Increasing Pore Size with Pressure and the Formation of a High-Pressure Phase at 1.47 GPa. *Angew. Chem. Int. Ed.* **2009**, *48*, 7087–7089.

31. Bennett, T.D.; Tan, J.C.; Moggach, S.A.; Galvelis, R.; Mellot-Draznieks, C.; Reisner, B.A.; Thirumurugan, A.; Allan, D.R.; Cheetham, A.K. Mechanical Properties of Dense Zeolitic Imidazolate Frameworks (ZIFs): A High-Pressure X-ray Diffraction, Nanoindentation and Computational Study of the Zinc Framework $Zn(Im)_2$, and its Lithium-Boron Analogue, $LiB(Im)_4$. *Chem. Eur. J.* **2010**, *16*, 10684–10690.

32. Fairen-Jimenez, D.; Moggach, S.A.; Wharmby, T.; Wright, P.A.; Parsons, S.; Düren, S. Opening the Gate: Framework Flexibility in ZIF-8 Explored by Experiments and Simulations. *J. Am. Chem. Soc.* **2011**, *133*, 8900–8902.

33. Tan, J.C.; Bennett, T.D.; Cheetham, A.K. Chemical structure, network topology, and porosity effects on the mechanical properties of Zeolitic Imidazolate Frameworks. *Proc. Natl. Acad. Sci. USA* **2010**, *107*, 9938–9943.

34. Tan, J.C.; Cheetham, A.K. Mechanical properties of hybrid inorganic–organic framework materials: Establishing fundamental structure–property relationships. *Chem. Soc. Rev.* **2011**, *40*, 1059–1080.

35. Tan, J.C.; Civalleri, B.; Lin, C.C.; Valenzano, L.; Galvelis, R.; Chen, P.F.; Bennett, T.D.; Mellot-Draznieks, C.; Zicovich-Wilson, C.M.; Cheetham, A.K. Exceptionally Low Shear Modulus in a Prototypical Imidazole-Based Metal-Organic Framework. *Phys. Rev. Lett.* **2012**, *108*, 095502.

36. Tan, J.C.; Civalleri, B.; Erba, A.; Albanese, E. Quantum mechanical predictions to elucidate the anisotropic elastic properties of zeolitic imidazolate frameworks: ZIF-4 vs. ZIF-zni. *CrystEngComm* **2015**, *17*, 375–382.

37. Ryder, M.R.; Tan, J.C. Explaining the mechanical mechanisms of zeolitic metal–organic frameworks: Revealing auxeticity and anomalous elasticity. *Dalton Trans*. **2016**, *45*, 4154–4161.

38. Ortiz, A.U.; Boutin, A.; Fuchs, A.H.; Coudert, F.X. Investigating the Pressure-Induced Amorphization of Zeolitic Imidazolate Framework ZIF-8: Mechanical Instability Due to Shear Mode Softening. *J. Phys. Chem. Lett.* **2013**, *4*, 1861–1865.

39. Su, Z.; Miao, Y.R.; Mao, S.M.; Zhang, G.H.; Dillon, S.; Miller, J.T.; Suslick, K.S. Compression-Induced Deformation of Individual Metal−Organic Framework Microcrystals. *J. Am. Chem. Soc.* **2015**, *137*, 1750–1753.

40. Mortada, B.; Chaplais, G.; Veremeienko, V.; Nouali, H.; Marichal, C.; Patarin, J. Energetic Performances of ZIF-8 Derivatives: Impact of the Substitution (Me, Cl, or Br) on Imidazolate Linker. *J. Phys. Chem. C* **2018**, *122*, 3846–3855.

41. Chaplais, G.; Fraux, G.; Paillaud, J.L.; Marichal, C.; Nouali, H.; Fuchs, A.H.; Coudert, F.X.; Patarin, J. Impacts of the Imidazolate Linker Substitution (CH_3, Cl, or Br) on the Structural and Adsorptive Properties of ZIF-8. *J. Phys. Chem. C* **2018**, *122*, 26945–26955.

42. Chen, S.; Li, X.; Dong, E.; Lv, H.; Yang, X.; Liu, R.; Liu, B. Intrinsic and Extrinsic Responses of ZIF-8 under High Pressure: A Combined Raman and X-ray Diffraction Investigation. *J. Phys. Chem. C* **2019**, *123*, 29693–29707.

43. Chen, S.; Li, X.; Lv, H.; Dong, E.; Yang, X.; Liu, R.; Liu, B. Pressure-induced insertion and transformation of N_2 in the cavities of zeolitic imidazolate framework-8: A Raman study. *J. Raman. Spectrosc.* **2020**, *51*, 1230–1239.

44. Erkartal, M.; Durandurdu, M. Pressure-induced amorphization, mechanical and electronic properties of zeolitic imidazolate framework (ZIF-8). *Mater. Chem. Phys*. **2020**, *240*, 122222.

45. Tortora, M.; Zajdel, P.; Lowe, A.R.; Chorążewski, M.; Leão, J.B.; Jensen, G.V.; Bleuel, M.; Giacomello, A.; Casciola, C.M.; Meloni, S.; et al. Giant Negative Compressibility by Liquid Intrusion into Superhydrophobic Flexible Nanoporous Frameworks. *Nano Lett.* **2021**, *21*, 2848–2853.

46. Fraux, G.; Coudert, F.-X.; Boutin, A.; Fuchs, A.H. Forced intrusion of water and aqueous solutions in microporous materials: From fundamental thermodynamics to energy storage devices. *Chem. Soc. Rev.* **2017**, *46*, 7421–7437.

47. Fraux, G.; Boutin, A.; Fuchs, A.H.; Coudert, F.X. Structure, Dynamics, and Thermodynamics of Intruded Electrolytes in ZIF-8. *J. Phys. Chem. C* **2019**, *123*, 15589–1559.

48. Ortiz, G.; Nouali, H.; Marichal, C.; Chaplais, G.; Patarin, J. Energetic performances of the metal-organic framework ZIF-8 obtained using high pressure water intrusion-extrusion experiments. *Phys. Chem. Chem. Phys.* **2013**, *15*, 4888–4891.

49. Grosu, Y.; Gomes, S.; Renaudin, G.; Grolier, J.P.E.; Eroshenko, V.; Nedelec, J.M. Stability of zeolitic imidazolate frameworks: Effect of forced water intrusion and framework flexibility dynamics. *RSC Adv.* **2015**, *5*, 89498–89502.

50. Eroshenko, V.; Regis, R.C.; Soulard, M.; Patarin, J. Energetics: A New Field of Applications for Hydrophobic Zeolites. *J. Am. Chem. Soc.* **2001**, *123*, 8129–8130.

51. Yot, P.G.; Boudene, Z.; Macia, J.; Granier, D.; Vanduyfhuys, L.; Verstraelen, T.; Speybroeck, V.V.; Devic, T.; Serre, C.; Ferey, G.; et al. Metal–organic frameworks as potential shock absorbers: The case of the highly flexible MIL-53(Al). *Chem. Commun*. **2014**, *50*, 9462–9464.

52. Banlusan, K.; Antillon, E.; Strachan, A. Mechanisms of Plastic Deformation of Metal−Organic Framework-5. *J. Phys. Chem. C* **2015**, *119*, 25845–25852.

53. Banlusan, K.; Amornkitbamrung, V.J. Effects of Free Volume on Shock-Wave Energy Absorption in A Metal–Organic Framework: A Molecular Dynamics Investigation. *J. Phys. Chem. C* **2020**, *124*, 17027–17038.

54. Zhou, X.; Miao, Y.; Suslick, K.S.; Dlott, D.D. Mechanochemistry of Metal–Organic Frameworks under Pres-sure and Shock. *Acc. Chem. Res*. **2020**, *53*, 2806–2815.

55. Patil, S.P.; Shendye, P.; Markert, B. Molecular investigation of mechanical properties and fracture behavior of graphene aerogel. *J. Phys. Chem. B* **2020**, *124*, 6132–6139.

56. Patil, S.P.; Kulkarni, A.; Markert, B. Shockwave response of graphene aerogels: An all-atom simulation study. *Comput. Mater. Sci*. **2021**, *189*, 110252.

57. Yot, P.G.; Vanduyfhuys, L.; Alvarez, E.; Rodriguez, J.; Itíe, J.P.; Fabry, P.; Guillou, N.; Devic, T.; Beurroies, I.; Llewellyn, P.L.; et al. Mechanical energy storage performance of an aluminum fumarate metal–organic framework. *Chem. Sci.* **2016**, *7*, 446–450.

58. Carrington, E.J.; McAnally, C.A.; Fletcher, A.J.; Thompson, S.P.; Warren, M.; Brammer, L. Solvent-switchable continuous-breathing behaviour in a diamondoid metal–organic framework and its influence on CO_2 versus CH_4 selectivity. *Nat. Chem.* **2017**, *9*, 882–889.

59. Murdock, C.R.; Hughes, B.C.; Lu, Z.; Jenkins, D.M. Approaches for synthesizing breathing MOFs by exploiting dimensional rigidity. *Coord. Chem. Rev.* **2014**, *258–259*, 119–136.

60. Greaves, G.N.; Meneau, F.; Sapelkin, A.; Colyer, L.M.; Gwynn, I.; Wade, S.; Sankar, G. The Rheology of Collapsing Zeolites Amorphized by Temperature and Pressure. *Nat. Mater.* **2003**, *2*, 622–628.

61. Haines, J.; Levelut, C.; Isambert, A.; Hebert, P.; Kohara, S.; Keen, D.A.; Hamouda, T.; Andraul, D. Topologically Ordered Amorphous Silica Obtained from the Collapsed Siliceous Zeolite, Silicalite-1-F, A Step toward Perfect Glasses. *J. Am. Chem. Soc.* **2009**, *131*, 12333–12338.

62. Wang, L.; Wang, W.; Chen, L.; Shen, Z. Formation of a unique glass by spark plasma sintering of a zeolite. *J. Mater. Res.* **2009**, *24*, 3241–3245.

63. Hwang, G.C.; Shin, T.J.; Blom, D.A.; Vogt, T.; Lee, Y. Pressure-Induced Amorphization of Small Pore Zeolites—The Role of Cation-H_2O Topology and Antiglass Formation. *Sci. Rep.* **2015**, *5*, 15056.

64. Santoro, M.; Gorelli, F.; Haines, J.; Cambon, O.; Levelut, C.; Garbarino, G. Silicon carbonate phase formed from carbon dioxide and silica under pressure. *Proc. Natl. Acad. Sci. USA* **2011**, *108*, 7689–7692.

65. Santoro, M.; Gorelli, F.A.; Bini, R. Carbon enters silica forming a cristobalite-type $CO_2 - SiO_2$ solid solution. *Nat. Commun.* **2013**, *4*, 3761.

66. Santoro, M.; Gorelli, F.; Bini, R.; Salamat, A.; Garbarino, G.; Levelut, C.; Cambon, O.; Haines, J. High-Pressure Synthesis of a Polyethylene/Zeolite Nano-Composite Material. *Nat. Commun.* **2014**, *5*, 1557.

67. Coudert, F.X. Systematic investigation of the mechanical properties of pure silica zeolites: Stiffness, anisotropy, and negative linear compressibility. *Phys. Chem. Chem. Phys*. **2013**, *15*, 16012–16018.

68. Li, W.; Probert, M.R.; Kosa, M.; Bennett, T.D.; Thirumurugan, A.; Burwood, R.P.; Parinello, M.; Howard, J.A.; Cheetham, A.K. Negative Linear Compressibility of a Metal−organic Framework. *J. Am. Chem. Soc.* **2012**, *134*, 11940–11943.

69. Ortiz, A.U.; Boutin, A.; Fuchs, A.H.; Coudert, F.X. Anisotropic Elastic Properties of Flexible Metal-Organic Frameworks: How Soft are Soft Porous Crystals? *Phys. Rev. Lett.* **2012**, *109*, 195502.

70. Ortiz, A.U.; Boutin, A.; Fuchs, A.H.; Coudert, F.X. Organic Frameworks with Wine-Rack Motif: What Determines their Flexibility and Elastic Properties? *J. Chem. Phys.* **2013**, *138*, 174703.

71. Cai, W.; Katrusiak, A. Giant negative linear compression positively coupled to massive thermal expansion in a metal–organic framework. *Chem. Commun.* **2014**, *5*, 4337–4342.

72. Cai, W.; Gładysiak, A.; Anioła, M.; Smith, V.J.; Barbour, L.J.; Katrusiak, A. Giant Negative Area Compressibility Tunable in a Soft Porous Framework Material. *J. Am. Chem. Soc.* **2015**, *137*, 9296–9301.

73. Serra-Crespo, P.; Dikhtiarenko, A.; Stavitski, E.; Juan-Alcañiz, J.; Kapteijn, F.; Coudert, F.X.; Gascon, J. Experimental evidence of negative linear compressibility in the MIL-53 metal–organic framework family. *CrystEngComm* **2015**, *17*, 276–280.

74. Zeng, Q.; Wang, K.; Qiao, Y.; Li, X.; Zou, B. Negative Linear Compressibility Due to Layer Sliding in a Layered Metal−Organic Framework. *J. Phys. Chem. Lett.*, **2017**, *8*, 1436–1441.

75. Zeng, Q.; Wang, K.; Zou, B. Large Negative Linear Compressibility in $InH(BDC)_2$ from Framework Hinging. *J. Am. Chem. Soc.* **2017**, *139*, 15648–1565.

76. Zeng, Q.; Wang, K.; Zou, B. Negative Linear Compressibility Response to Pressure in Multitype Wine-Rack Metal−Organic Frameworks. *ACS Mater. Lett.* **2020**, *2*, 291–295.

77. Yan, Y.; O'Connor, A.E.; Kanthasamy, G.; Atkinson, G.; Allan, D.R.; Blake, A.J.; Schroder, M. Unusual and Tunable Negative Linear Compressibility in the Metal-Organic Framework MFM-133(M) (M = Zr, Hf). *J. Am. Chem. Soc.* **2018**, *140*, 3952–3958.

78. Feng, G.; Zhang, W.; Dong, L.; Li, W.; Cai, W.; Wei, W.; Ji, L.; Lin, Z.; Lu, P. Negative area compressibility of a hydrogen bonded two-dimensional material. *Chem. Sci.* **2019**, *10*, 1309–1315.

79. Chen, Z.; Xu, B.; Li, Q.; Meng, Y.; Quan, Z.; Zou, B. Selected Negative Linear Compressibilities in the Metal−Organic Framework of $[Cu(4,4' - bpy)_2 (H_2O)_2] \cdot SiF_6$. *Inorg. Chem.* **2020**, *59*, 1715–1722.

80. Zajdel, P.; Chorążewski, M.; Leão, J.B.; Jensen, G.V.; Bleuel, M.; Zhang, H.F.; Feng, T.; Luo, D.; Li, M.; Lowe, A.R.; et al. Inflation Negative Compressibility during Intrusion−Extrusion of a Non-Wetting Liquid into a Flexible Nanoporous Framework. *Phys. Chem. Lett.* **2021**, *12*, 4951–4957.

81. Colmenero, F. Negative Linear Compressibility in Nanoporous Metal–Organic Frameworks Rationalized by the Empty Channel Structural Mechanism. *Phys. Chem. Chem. Phys.* **2021**, *23*, 8508–8524.

82. Colmenero, F.; Lobato, A.; Timón, V. Compressing the Channels in the Crystal Structure of Copper Squarate Metal-Organic Framework. *Solids* **2022**, *3*, 374–384.

83. Colmenero, F.; Lobato, A.; Timón, V. Mechanical Characterization of Anhydrous Microporous Aluminophosphate Materials: Tridimensional Incompressibility, Ductility, Isotropy and Negative Linear Compressibility. *Solids* **2022**, *3*, 457–499.

84. Grima, J.N.; Jackson, R.; Alderson, A.; Evans, K.E. Do Zeolites Have Negative Poisson's Ratios? *Adv. Mater.* **2000**, *12*, 1912–1918.

85. Grima, J.N.; Gatt, R.; Zammit, V.; Williams, J.J.; Evans, K.E.; Alderson, A.; Walton, R.I. Natrolite: A Zeolite with Negative Poisson's Ratios. *J. Appl. Phys.* **2007**, *101*, 086102.

86. Evans, J.D.; Coudert, F.X. Predicting the Mechanical Properties of Zeolite Frameworks by Machine Learning. *Chem. Mater.* **2017**, *29*, 7833–7839.

87. Gaillac, R.; Chibani, S.; Coudert, F.X. Speeding up discovery of auxetic zeolite frameworks by machine learning. *Chem. Mater.* **2020**, *32*, 2653–2663.

88. Baughman, R.H.; Stafstrom, S.; Cui, C.; Dantas, S.O. Compressibilities in One or More Dimensions. *Science* **1998**, *279*, 1522–1524.

89. Cairns, A.B.; Goodwin, A.L. Negative Linear Compressibility. *Phys. Chem. Chem. Phys.* **2015**, *17*, 20449–20465.

90. Lakes, R.S. Foam Structures with a Negative Poisson's Ratio. *Science* **1987**, *235*, 1038–1040.

91. Lakes, R.S. Negative-Poisson's-Ratio Materials: Auxetic Solids. *Annu. Rev. Mater. Res.* **2017**, *47*, 63–81.

92. Nicolaou, Z.G.; Motter, A.E. Mechanical metamaterials with negative compressibility transitions. *Nat. Mater.* **2012**, *11*, 608–613.

93. Spinks, G.M.; Wallace, G.G.; Fifield, L.S.; Dalton, L.R.; Mazzoldi, A.; De Rossi, D.; Khayrullin, I.; Baughman, R.H. Pneumatic Carbon Nanotube Actuators. *Adv. Mater.* **2002**, *14*, 1728–1732.

94. Aliev, A.E.; Oh, J.; Kozlov, M.E.; Kuznetsov, A.A.; Fang, S.; Fonseca, A.F.; Ovalle, R.; Lima, M.D.; Haque, M.H.; Gartstein, Y.N.; et al. Giantstroke, superelastic carbon nanotube aerogel muscles. *Science* **2009**, *323*, 1575–1578.

95. Evans, K.E.; Alderson, A. Auxetic Materials: Functional Materials and Structures from Lateral Thinking! *Adv. Mater.* **2000**, *12*, 617–628.

96. Fang, N.; Xi, D.; Xu, J.; Ambati, M.; Srituravanich, W.; Sun, C.; Zhang, X. Ultrasonic metamaterials with negative modulus. *Nat. Mater.* **2006**, *5*, 452–456.

97. Uhoya, W.; Tsoi, G.; Vohra, Y.K.; McGuire, M.A.; Sefat, A.S.; Sales, B.C.; Mandrus, D.; Weir, S.T. Anomalous compressibility effects and superconductivity of $EuFe_2As_2$ under high pressures. *J. Phys. Condens. Matter.* **2010**, *22*, 292202.

98. Jiang, X.; Molokeev, M.S.; Dong, L.; Dong, Z.; Wang, N.; Kang, L.; Li, X.; Li, Y.; Tian, C.; Peng, S.; et al. Anomalous mechanical materials squeezing three-dimensional volume compressibility into one dimension. *Nat. Commun.* **2020**, *11*, 5593.

99. Astala, R.; Auerbach, S.M.; Monson, P.A. Density Functional Theory Study of Silica Zeolite Structures: Stabilities and Mechanical Properties of SOD, LTA, CHA, MOR, and MFI. *J. Phys. Chem. B* **2004**, *108*, 9208–9215.

100. Astala, R.; Auerbach, S.M.; Monson, P.A.; Normal mode approach for predicting the mechanical properties of solids from first principles: Application to compressibility and thermal expansion of zeolites. *Phys. Rev. B* **2005**, *71*, 014112.

101. Bahr, D.F.; Reid, J.A.; Mook, W.M.; Bauer, C.A.; Stumpf, R.; Skulan, A.J.; Moody, N.R.; Simmons, B.A.; Shindel, M.M.; Allendorf, M.D. Mechanical properties of cubic zinc carboxylate IRMOF-1 metal-organic framework crystals. *Phys. Rev. B* **2007**, *76*, 184106.

102. Colmenero, F. Anomalous mechanical behavior of the deltic, squaric and croconic cyclic oxocarbon acids. *Mater. Res. Express* **2019**, *6*, 045610.

103. Colmenero, F. Mechanical properties of anhydrous oxalic acid and oxalic acid dihydrate. *Phys. Chem. Chem. Phys.* **2019**, *21*, 2673–2690.

104. Colmenero, F. Organic acids under pressure: Elastic properties, negative mechanical phenomena and pressure induced phase transitions in the lactic, maleic, succinic and citric acids. *Mater. Adv.* **2020**, *1*, 1399–1426.

105. Colmenero, F.; Cobos, J.; Timón, V. Negative linear compressibility in uranyl squarate monohydrate. *J. Phys. Cond. Matter.* **2019**, *31*, 175701.

106. Colmenero, F.; Timón, V. Extreme negative mechanical phenomena in the zinc and cadmium anhydrous metal oxalates and lead oxalate dihydrate. *J. Mater. Sci.* **2020**, *55*, 218–236.

107. Colmenero, F. Silver oxalate: Mechanical properties and extreme negative mechanical phenomena. *Adv. Theor. Simul.* **2019**, *2*, 1900040.

108. Colmenero, F.; Jiang, X.; Li, X.; Li, Y.; Lin, Z. Negative area compressibility in silver oxalate. *J. Mater. Sci.* **2021**, *56*, 269–277.

109. Colmenero, F.; Cobos, J.; Timón, V. Periodic Density Functional Theory Study of the Structure, Raman Spectrum, and Mechanical Properties of Schoepite Mineral. *Inorg. Chem.* **2018**, *57*, 4470–4481.

110. Colmenero, F.; Fernández, A.M.; Cobos, J.; Timón, V. Becquerelite mineral phase: Crystal structure and thermodynamic and mechanical stability by using periodic DFT. *RSC Adv.* **2018**, *8*, 24599–24616.

111. Colmenero, F.; Plášil, J.; Sejkora, J. The layered uranyl silicate mineral uranophane-β: Crystal structure, mechanical properties, Raman spectrum and comparison with the α-polymorph. *Dalton Trans.* **2018**, *48*, 16722–16736.

112. Colmenero, F.; Plášil, J.; Cobos, J.; Sejkora, J.; Timón, V.; Čejka, J.; Bonales, L.J. Crystal structure, hydrogen bonding, mechanical properties and Raman spectrum of the lead uranyl silicate monohydrate mineral kasolite. *RSC Adv.* **2019**, *9*, 15323–15334.

113. Colmenero, F.; Plášil, J.; Sejkora, J. The crystal structures and mechanical properties of the uranyl carbonate minerals roubaultite, fontanite, sharpite, widenmannite, grimselite and čejkaite. *Inorg. Chem. Front.* **2020**, *7*, 4197–4221.

114. Payne, M.C.; Teter, M.P.; Ailan, D.C.; Arias, A.; Joannopoulos, J.D. Iterative minimization techniques for ab initio total-energy calculations: Molecular dynamics and conjugate gradients. *Rev. Mod. Phys.* **1992**, *64*, 1045–1097.

115. Clark, S.J.; Segall, M.D.; Pickard, C.J.; Hasnip, P.J.; Probert, M.I.J.; Refson, K.; Payne, M.C. First Principles Methods Using CASTEP. *Z Kristallogr.* **2005**, *220*, 567–570.

116. MaterialsStudio. Available online: https://3dsbiovia.com/products/collabo-rative-science/biovia-materials-studio/ (accessed on 15 June 2022).

117. Perdew, J.P.; Burke, K.; Ernzerhof, M. Generalized Gradient Approximation Made Simple. *Phys. Rev. Lett.* **1996**, *77*, 3865–3868.

118. Grimme, S. Semiempirical GGA-type Density Functional Constructed with a Long-Range Dispersion Correction. *J. Comput. Chem.* **2006**, *27*, 1787–1799.

119. Troullier, N.; Martins, J.L. Efficient Pseudopotentials for Plane-Wave Calculations. *Phys. Rev. B* **1991**, *43*, 1993–2006.

120. Monkhorst, H.J.; Pack, J.D. Special Points for Brillouin-zone Integration. *Phys. Rev. B* **1976**, *13*, 5188–5192.

121. Pfrommer, B.G.; Cote, M.; Louie, S.G.; Cohen, M.L. Relaxation of Crystals with the Quasi-Newton Method. *J. Comput. Phys.* **1997**, *131*, 233–240.
122. Downs, R.T.; Bartelmehs, K.L.; Gibbs, G.V.; Boisen, M.B. Interactive software for calculating and displaying X-ray or neutron powder diffractometer patterns of crystalline materials. *Am. Mineral.* **1993**, *78*, 1104–1107.
123. Yu, R.; Zhu, J.; Ye, H.Q. Calculations of Single-Crystal Elastic Constants Made Simple. *Comput. Phys. Commun.* **2010**, *181*, 671–675.
124. Colmenero, F. Revealing Rutherfordine Mineral as an Auxetic Material. *Appl. Sci.* **2018**, *8*, 2281.
125. Reticular Chemistry Structure Resource (RSCR). Available online: http://rcsr.anu.edu.au/home (accessed on 15 September 2022).
126. Mouhat, F.; Coudert, F.X. Necessary and Sufficient Elastic Stability Conditions in Various Crystal Systems. *Phys. Rev. B* **2014**, *90*, 224104.
127. Marmier, A.; Lethbridge, Z.A.D.; Walton, R.I.; Smith, C.W.; Parker, S.C.; Evans, K.E. ElAM: A Computer Program for the Analysis and Representation of Anisotropic Elastic Properties. *Comput. Phys. Commun.* **2010**, *181*, 2102–2115.
128. Colmenero, F.; Sejkora, J.; Plášil, J. Crystal structure, infrared spectrum and elastic anomalies in tuperssuatsiaite. *Sci. Rep.* **2020**, *10*, 7510.
129. Spackman, R.; Grosjean, A.; Thomas, S.P.; Karothu, D.P.; Naumov, P.; Spackman, M.A. Quantifying Mechanical Properties of Molecular Crystals: A Critical Overview of Experimental Elastic Tensors. *Angew. Chem. Int. Ed.* **2022**, *61*, e202110716.
130. Yot, P.G.; Ma, Q.; Haines, J.; Yang, Q.; Ghoufi, A.; Devic, T.; Serre, C.; Dmitriev, V.; Férey, G.; Zhong, C.; et al. Mechanical behaviour of the MIL-47(V) Metal Organic Frameworks: A joint experimental-modeling approach. *Chem. Sci.* **2012**, *3*, 1100–1104.
131. Karagiaridi, O.; Lalonde, M.B.; Wojciech, B.; Sarjeant, A.A.; Farha, O.K.; Hupp, J.T. Opening ZIF-8: A Catalytically Active Zeolitic Imidazolate Framework of Sodalite Topology with Unsubstituted Linkers. *J. Am. Chem. Soc.* **2012**, *134*, 18790–18796.